Journal of Marine Research, 73, 153–184, 2015

Low-frequency variability of the separated western boundary current in response to a seasonal wind stress in a 2.5-layer model with outcropping

by Jérôme Sirven[1], Sabine Février[2], and Christophe Herbaut[3]

ABSTRACT

The response of the separated western boundary current to a seasonally varying wind stress is studied in a 2.5-layer model where the second layer outcrops. The model is eddy permitting with a resolution of one-sixth of a degree, and the geometry of the basin is idealized. The response is studied for two mean states: the first one is only wind driven, whereas the second one takes into account the existence of a meridional overturning circulation. The separation latitude and the mean path followed by the separated western boundary current are shifted northward of approximately 2° when the overturning circulation is added. Though the mean states are significantly different, the variability of the current shows quite similar characteristics. The seasonal lateral shifts of the outcrop line always remain small, scarcely exceeding 0.2°. On the contrary, interannual shifts that can peak up to approximately 1° to 2° are observed. This variability is associated with the development of nonlinear waves along the outcrop line. The corresponding timescales extend on a broad range of periods (longer than approximately 4 years), with an energy maximum depending on the set up. A simple analytical model derived from the 2.5-layer model allows us to explain which mechanism drives the propagation of these waves.

Keywords: low frequency variability, separated western boundary current, nonlinear wave, outcropping

1. Introduction

The circulation of the North Atlantic Ocean is dominated by the Gulf Stream, which separates from the American coast at 35° N (Cape Hatteras), meanders toward the Grand Banks, and then splits into two main branches, the branch flowing to the northeast being known as the North Atlantic Current. The Gulf Stream is the basic pattern of the ocean circulation of the North Atlantic Ocean and probably the most observed and studied current of the world's ocean. However, despite these observations and studies, neither the separation

LOCEAN/IPSL, Université Pierre et Marie Curie, Tour 45, étage 4, CC 100, 4 place Jussieu, 75252 Paris CEDEX 05, France.

1. Corresponding author: ***e-mail: jerome.sirven@locean-ipsl.upmc.fr***
2. ***e-mail: sabine.fevrier@locean-ipsl.upmc.fr***
3. ***e-mail: christophe.herbaut@locean-ipsl.upmc.fr***

mechanism from the coast at 35° N nor the mechanism driving the large-scale shifts of its axis at seasonal and interannual timescales are completely understood.

Halkin and Rossby (1985) calculated the transport above 2,000 m at 73° W from in situ measurements between September 1980 and May 1983 and showed that their results were consistent with an annual cycle, peaking in April, in agreement with Worthington (1976). They obtained this result by comparing two subsets of transport: those calculated from data collected between February and July and those calculated for the other half of the year. A statistical (Wilcoxian) test showed that they were significantly different. Kelly, Singh, and Huang (1999) studied 4 years of altimetric sea surface height data and found that the Gulf Stream shows seasonal variations in surface transport and latitudinal position. The latitudinal shifts occur in a range of 0.42°, being more pronounced west of 63° W. However, depending on the period, the data (TOPEX or GEOSAT), and the location (east or west of 63° W), the explained percentage of variance varied from 3% to 72%. Contrasting with these results, Taylor and Stephens (1998) or Frankignoul et al. (2001), using various products issued from in situ or satellite observations, did not find any consistent seasonal signal in the shifts of the Gulf Stream.

The interannual variability perhaps leads to less conflicting results. The signal is stronger than the seasonal one and seems to be correlated with the North Atlantic Oscillation (NAO; Taylor and Stephens 1998; Joyce, Deser, and Spall 2000; Frankignoul et al. 2001) and to the Slope Water properties (Peña-Molino and Joyce 2008). Slope Water variations are usually associated with time-varying outflow from the Labrador shelf regions (Rossby and Benway 2000; Rossby, Flagg, and Donohue 2005). However, the respective roles of wind or buoyancy forcings still remain controversial. For example, Hameed and Piontkovski (2004) showed that the position of the Gulf Stream "north wall" was mostly influenced by the Icelandic low and lagged its pressure anomalies by 1–3 years. They consequently emphasized the role of Labrador Sea variability on the Gulf Stream shifts and considered that the direct impact of wind stress variability (at least over the subtropical gyre) on the Gulf Stream path was negligible (see also Peña-Molino and Joyce 2008).

Paralleling these studies based on observations, various theories have been proposed to explain how the path of the Gulf Stream may be affected. The role of the deep western boundary current has been pointed out in several studies. For example, Thompson and Schmitz (1989) linked the separation point of the Gulf Stream to the southward transport of the deep western boundary current, and Spall (1996a, 1996b) showed that the shifts of the separation point could be due to the amount of Labrador Sea Water at the crossover point. More recently, Zhang and Vallis (2007) pointed out the role of bottom vortex stretching on the path of the North Atlantic western boundary current and on the northern recirculation gyre.

Inertial effects have been also examined: Marshall and Nurser (1988) suggested that a balance between forcing and dissipation drives the dynamics of the recirculation gyre, and Cessi (1990) showed that the latitude of separation of the Gulf Stream could depend on the latter (see also Cessi, Condie, and Young 1990; Chassignet, Bleck, and Rooth 1995; Özgökmen, Chassignet, and Paiva 1997, etc.).

The role of the outcropping of the isopycnal surfaces was first emphasized by Charney (1955) and then studied by Parsons (1969). Afterward, Chassignet and Bleck (1993) studied in a series of numerical experiments the latitude of the separation point and showed that as soon as the upper/lower layer ratio is small enough, the separation occurs south of the zero wind stress curl line, in agreement with the theory. The diabatic mechanisms were not considered in their study. However, Pedlosky (1987) or Nurser and Williams (1990) have shown that diabatic heating or cooling could modify the Parsons separation mechanism. Chassignet, Bleck, and Rooth (1995) introduced a mixed layer to take into account these diabatic processes and showed that their previous results were modified: the underlying layers outcrop in the mixed layer where the horizontal density gradient is maximum.

These studies used a stationary forcing and focused on the mean position of the western boundary current and the intensity of the transport. The consequences of the variability of the wind forcing were considered by Sirven (2005), who extended the 1.5-layer model of Huang and Flierl (1987) to the time-dependent case and showed that the lateral shifts of the Gulf Stream could depend on the wind stress variations. These shifts—computed from the position of the line where the motionless second layer outcrops—show a lag of 0 to 4 years with the forcing. This lag results from a combination of the instantaneous Ekman response and the delayed response due to Rossby wave propagation. Note that other studies, based on low-resolution ocean general circulation models (see, for example, de Coëtlogon et al. 2006), also found correlations between wind stress variations (linked to the NAO) and lateral shifts of the Gulf Stream.

The fact that the response of the ocean to the NAO may be studied independently of its possible feedback on the atmosphere is not obvious. The approach followed by Marshall, Johnson, and Goodman (2001) considered this point; they developed a simple mathematical model to study the interaction of the NAO with the ocean circulation. Their study suggested that, adding to its impact on the ocean gyres, the NAO forcing introduced local anomalies in overturning circulation (with timescales less than a decade), which, in turn, might introduce delay timescales through a mechanism of delayed oscillator.

An approach based on the theory of nonlinear dynamical systems has also been initiated for about 20 years (see Simonnet et al. [2003a, 2003b] for an analysis of a 2.5-layer model without outcropping and Primeau and Newman [2007] for that of a 1.5-layer model with outcropping). These analyses explore how the different regimes of models depend on the parameters they contain (intensity of the mean wind stress, Froude number, etc.). Their results suggest the existence of peaks of variability, which can be associated with the nonlinear behavior of the model, after local or global bifurcations. Usually, the forcing fields are stationary in these approaches. To our knowledge, the influence of a time-varying forcing has only been investigated by Shimokawa and Matsuura (2010). Using a 1.5-layer quasi-geostrophic model, they showed that synchronization appeared between an intrinsic frequency of the system and half the frequency of the forcing; on the other hand, intermittency (irregular variations) emerged with an increasing amplitude of the forcing.

The approach we follow here is closer to that developed in a series of studies by Sasaki and coauthors (Sasaki and Schneider 2011a, 2011b; Sasaki, Minobe, and Schneider 2013). They used the thin-jet theory to explain the decadal variability of the Gulf Stream and Kuroshio Extension. They observed, using an eddy-resolving general circulation model, that the meridional shifts of the Gulf Stream or the Kuroshio originated in the open ocean over the jet axis and propagated westward along the latter. They showed that the thin-jet model successfully reproduced the propagations and shifts of the jet latitude simulated by the model.

It is highly probable that all the processes previously summarized contribute to the dynamics of separated western boundary currents. In this study, we concentrate on the low-frequency variability of the separated western boundary current in response to seasonal forcings and try to examine which mechanisms operate on this timescale. A 2.5-layer model where outcropping is allowed is used for this purpose. Indeed, such a model is sufficiently complex to include most of the mechanisms previously described but remains sufficiently simple to perform various experiments integrated on a long time period (120 years).

The model and the experimental setup are described in Section 2. A regular grid resolution of one-sixth of a degree is used (eddy permitting model), which allows us to represent the steep gradients of thickness close to the outcrop line. In Section 3, the mean state and the seasonal variability of the model are briefly described for each experiment. In Section 4, the interannual variability of the model response is studied. A simple nonlinear model that explains the results of Section 4 is developed and analyzed in Section 5; in particular, we draw a comparison between this model and the thin-jet theory stated in a series of studies by Sasaki and coauthors (Sasaki and Schneider 2011a, 2011b; Sasaki, Minobe, and Schneider 2013). Section 6 summarizes and discusses the results.

2. The model setup

a. Description of the model

We use a reduced gravity model with two active layers of constant density over an infinite layer at rest. It extends from 70° W to 10° W in longitude and from 15° N to 55° N in latitude. Along the western side, the coast is crudely represented. A realistic wind stress can thus be used over the whole ocean basin (see Section 2b), which would be difficult otherwise: indeed, as the wind stress curl is much stronger over the continents than over the ocean, it would induce an unrealistic response of the ocean.

The thickness of the surface (mid)layer is noted $h_1(h_2)$, and its velocity $\mathbf{v}_1(\mathbf{v}_2)$. At rest, $h_1 = 450$ m and $h_2 = 950$ m. Chassignet and Bleck (1993) showed that the midlatitude jet separates further south when the ratio between the upper and lower layer thicknesses decreases. We performed a series of experiments (not shown) with different first-layer thicknesses (from 350 m to 550 m) to verify that this property is actually reproduced in our model. The thicknesses at rest in the model thus result from a compromise between the

desire to have a current detached from the coast and a recirculation area to the north of its path, and the necessity to keep the first layer sufficiently deep in the subtropical gyre.

The momentum conservation equation is as follows:

$$\frac{\partial \mathbf{v}_i}{\partial t} + (\mathrm{curl}\mathbf{v}_i + f)\mathbf{n} \wedge \mathbf{v}_i = -\mathbf{grad}(B_i) + \nu \Delta_H \mathbf{v}_i + \frac{\boldsymbol{\tau}_{i-1} - \boldsymbol{\tau}_i}{h_i} \tag{1}$$

with $i = 1$ (surface layer) or $i = 2$ (midlayer), and $\mathbf{n}$ is a vector normal to the Earth's surface. The Bernouilli function B_i is respectively equal to $B_1 = 2bh_1 + bh_2 + \mathbf{v}_1^2/2$ and $B_2 = bh_1 + bh_2 + \mathbf{v}_2^2/2$, where the reduced gravity b is equal to 0.004 m s^{-2} (to obtain these simple expressions, we assumed that the differences of density between the successive layers were the same: "$\rho_3 - \rho_2 = \rho_2 - \rho_1$"). The surface wind stress is $\rho_0 \boldsymbol{\tau}_0$, and the Reynolds stress at the interface is $\rho_0 \boldsymbol{\tau}_1 = \rho_0 k(\mathbf{v}_1 - \mathbf{v}_2)$ ($\rho_0 = 1{,}000$ kg m^{-3}). There is no stress between the midlayer and the layer at rest: $\boldsymbol{\tau}_2 = 0$.

The mass conservation equation is as follows:

$$\frac{\partial h_i}{\partial t} + \mathrm{div}(h_i \mathbf{v}_i) = w_{ei} \tag{2}$$

where $w_{e1} = 0$ and w_{e2} represents a possible mass flux into the second layer. This term allows us to introduce a "meridional overturning circulation" in the model as explained in Section 2b.

The previous equations are solved by finite differences on a C-grid on the sphere. The spatial scheme preserves enstrophy, following Sadourny (1975). Free slip boundary conditions are applied, and the gradients of h_1 and h_2 vanish perpendicularly to the boundary. No dissipation is added in the continuity equations, and mass is conserved by the numerical scheme. The time integration is performed using a modified leapfrog scheme with an Asselin filter. Details on the numerical scheme are given in the Appendix. The time step is equal to 15 minutes, the viscosity coefficient ν is equal to 400 m^{2}s^{-1}, and the friction coefficient k is equal to 8×10^{-5} m s^{-1} in all the experiments.

b. The wind stress forcing and the experimental setup

The wind stress comes from the ERA-40 reanalysis (Uppala et al. 2005), which covers the period ranging from 1958 to 2001. The monthly wind stress climatology has been computed and used to perform a 200-year spin-up experiment, until the model no longer shows a significant drift.

Figure 1 shows the wind stress (arrows) and the wind stress curl (color) in January and July. The strongest values in winter are found around 65° W, 48° N ($\simeq$0.4 Pa) on the land. Over the ocean, the wind stress does not exceed 0.25 Pa in winter and is much weaker in summer, approximatively divided by a factor of 2.

The mean Ekman pumping (Fig. 2, bottom panel) is upward (downward) north (south) of a tilted line going from 35° N at the western side to 52° N at 24° W. It peaks at approximately

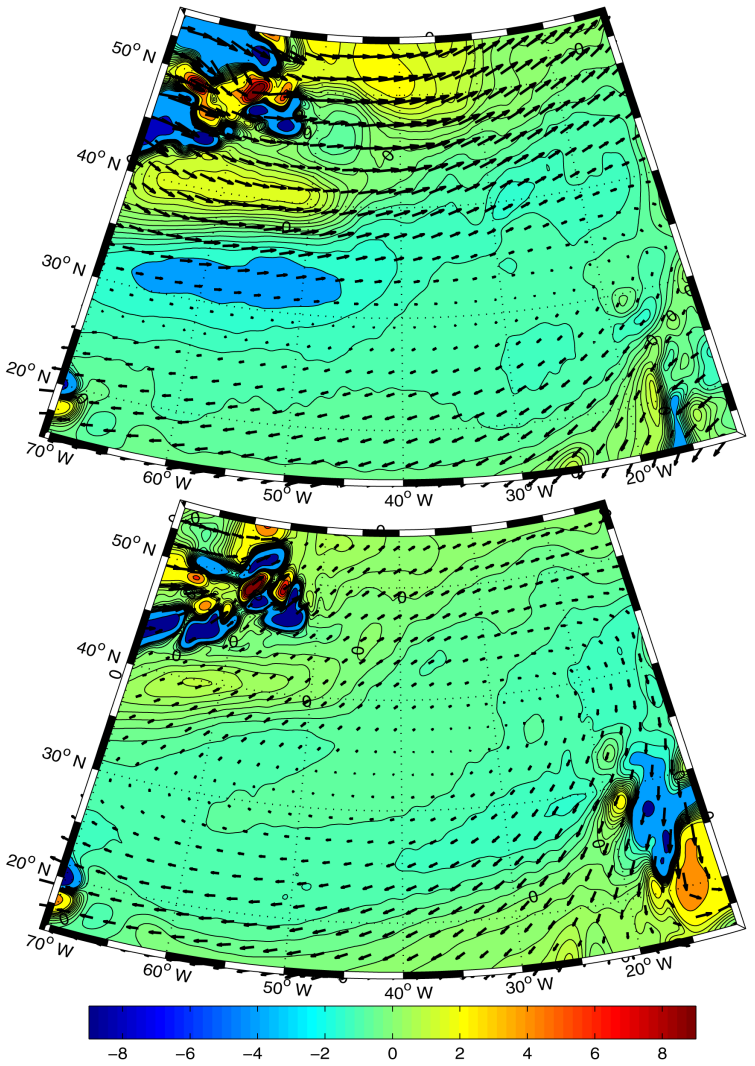

Figure 1. Arrows: Mean wind stress in January (top) and July (bottom). The maximum in January peaks at 0.4 Pa. Colors: corresponding values of the wind stress curl (units: 10^{-7} Pa m^{-1}). Note that the large values in the northwestern part of the basin are on land; similarly, the values peaking at approximately 0.3 Pa in July around 15° W, 20° N are over Africa. Over the ocean, the wind stress is approximately 0.1–0.2 Pa.

10^{-6} m s^{-1} (31 m y^{-1}). The seasonal variability is illustrated in the same figure, with the middle and top panels showing the first principal component (PC) and the corresponding empirical orthogonal function (EOF) of the Ekman pumping anomalies computed from the monthly climatology. The first PC represents 66% of the seasonal variance. It shows that

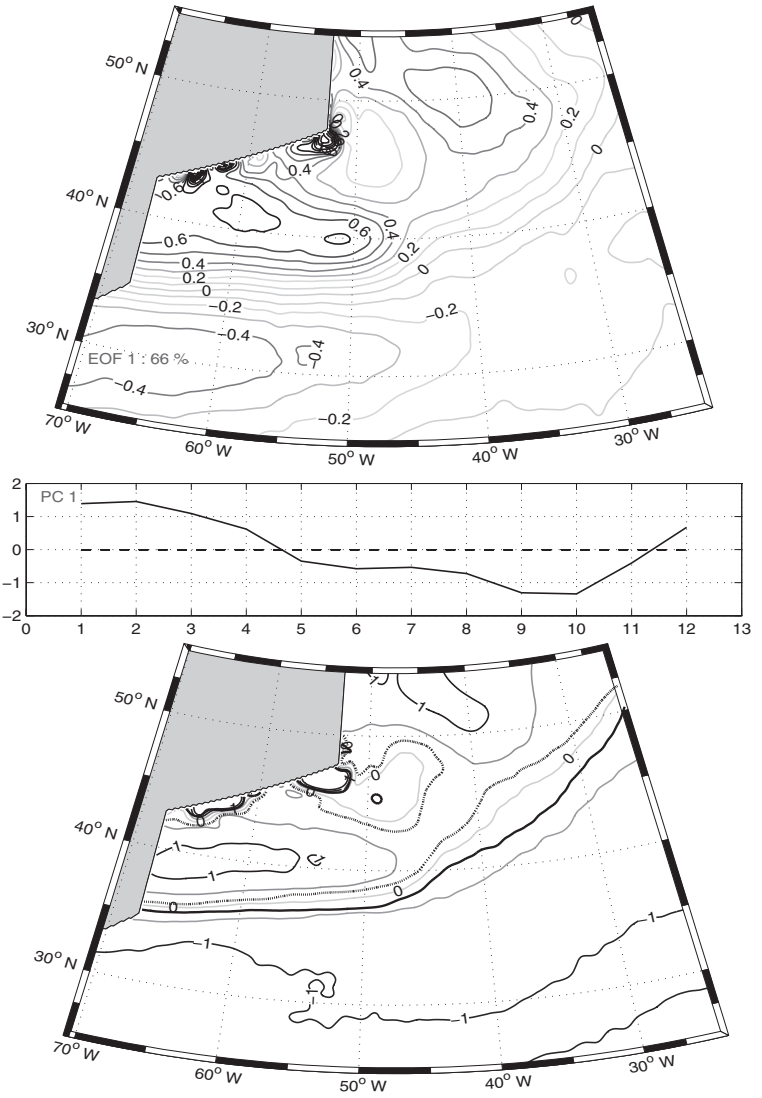

Figure 2. First EOF (top) and the corresponding PC (middle) of the Ekman pumping anomalies computed from the monthly climatology; the PC is normalized. Mean Ekman pumping (units: 10^{-6} m s^{-1}, bottom). The black bold line (black dotted line) shows the zero Ekman pumping line for "Mean + 1.3 × EOF" ("Mean − 1.3 × EOF"). EOF, empirical orthogonal function; PC, principal component.

the Ekman pumping is strong from December to April with a peak in February. The black bold and black dotted lines in the bottom panel of Figure 2 allow us to visualize the shifts of the zero Ekman pumping line. The shifts remain moderate in the western part of the basin (the line shifts southward in winter by approximately 1°) but are large east of around 42° W, reaching 3° to 4° at 39° W.

Note that all the EOFs shown in this article are computed over the same reduced domain around the separated western boundary current in order to enhance legibility. We have verified for all the figures that the EOFs were not modified when the computations were done on the whole domain.

After a 200-year spin-up with the previous setup, three experiments were made; each experiment lasts 140 years, but only the last 120 years are analyzed in order to eliminate the influence of the initial state.

In the reference experiment, the model is integrated with the monthly climatology of the wind stress we have just described. In a first sensitivity experiment, hereafter referred to as the stationary experiment, the seasonal cycle of the wind stress is removed, leading to a stationary forcing field. In a second one, referred to as the overturning experiment, a constant downward mass flux of 5.75 Sv is prescribed in the northern part of the basin at the basis of the second layer (between 52° N and 55° N, and from the western boundary to 35° W), the wind stress being that of the reference experiment. This downward flux is balanced by an upward flux that acts over the whole basin. These fluxes aim at representing a meridional overturning circulation.

The classical estimation of the Atlantic meridional overturning circulation ranges between 15 and 20 Sv. Only a part of this meridional transport is modeled in the overturning experiment: it corresponds to the observed variations of the meridional transport between the limits of the model (15° N and 55° N), which can be estimated between 4 and 7 Sv. This range is based on the results of Lumpkin and Speer (2007, fig. 3), as shown in their figure 3 (middle panel), and Talley, Reid, and Robbins (2003). It is estimated by considering that the second layer of our model represents isopycnal layers between approximately 27 σ_θ and 27.6 σ_θ. The value we have chosen (5.75 Sv) lies in this range and generates important changes of the mean state. Note that for all three experiments there is no year-to-year variability in the wind stress forcing.

3. Mean state and seasonal variability

a. The reference experiment

The mean state and the seasonal variability in the reference experiment are illustrated by Figures 3 and 4. As expected, the second layer outcrops in the northwestern part of the basin. This outcropping is associated with a cyclonic flow that mimicks the subpolar gyre. South, there is an anticyclonic gyre where the first layer deepens westward, the thickness increasing from approximately 400 m at the eastern side to approximately 800 m at the western side. These thickness variations of the first layer are approximatively compensated

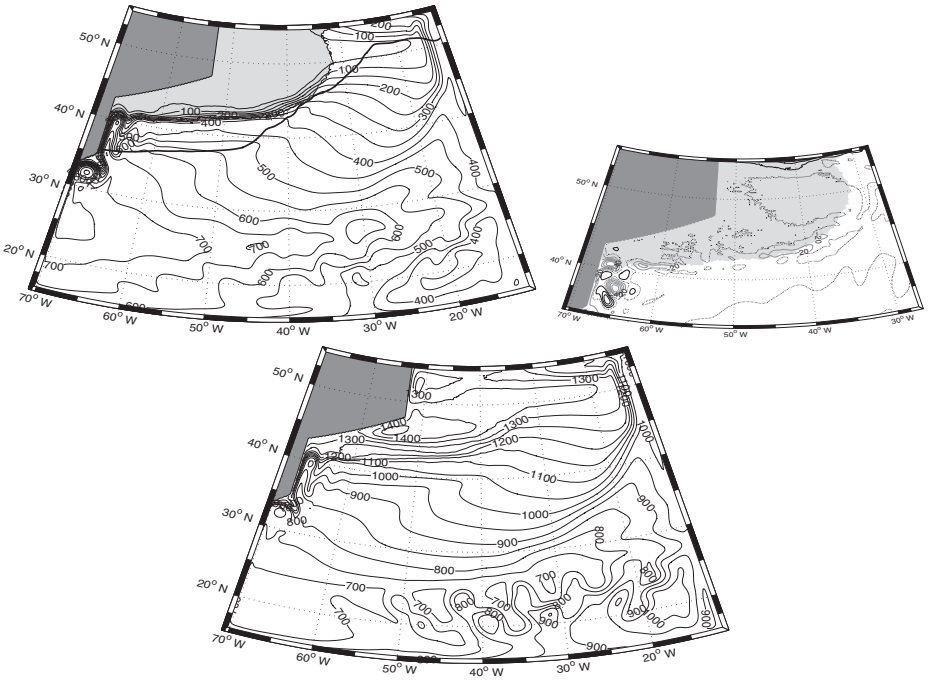

Figure 3. January mean of the first-layer thickness h_1 (top). The black bold line shows the mean zero Ekman pumping line. Differences between the July and January means of h_1 (middle) in the separated western boundary current area. The outcrop area is grayed out in both panels. January mean of the second-layer thickness h_2 (bottom). The means have been computed from the last 120 years of the experiment (units: m).

by those of the second layer so that the total thickness of the two active layers remains close to 1,400 m.

North of 32° N, in the surface layer, a boundary current follows the coast toward the north, then splits into two branches (Fig. 4). At 37° N, the first branch separates from the main stream and flows eastward, approximatively along the zero Ekman pumping line. Further north, at around 40° N, the boundary current veers eastward, following the outcrop line, and forms the second branch, which is well detached from the northern coast and is stronger than the first one. Below this branch, in the second layer, a strong eastward current is also observed.

As in most simple models (e.g., Chassignet and Bleck 1993, fig. 7; Simonnet et al. 2003b, fig. 15, etc.), a permanent boundary eddy forms. Here, it is located at 32° N (Fig. 3) because of the shape of the coastline that deflects the current. However, it does not help the current to separate from the coast; this means that the "vorticity crisis" mechanism is not at work here.

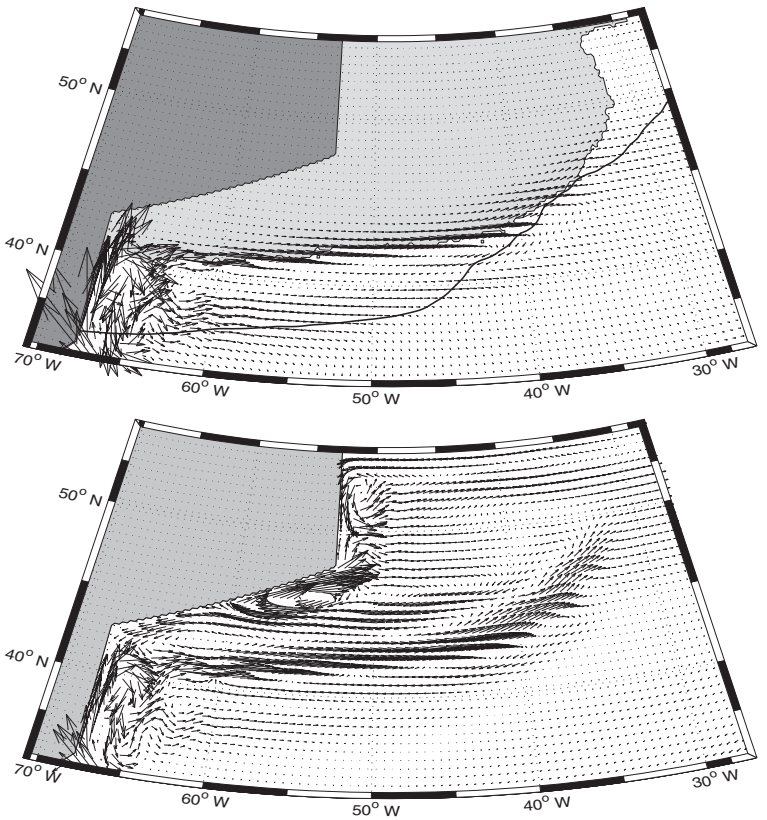

Figure 4. Annual mean transports in the first (top; longest arrow: 3.2 Sv) and second (bottom; longest arrow: 1.8 Sv) layers. The zero Ekman pumping line is shown by the black bold line. The means have been computed from the last 120 years of the reference experiment.

Note that the loss of potential vorticity in the subtropical gyre is balanced by a gain in the boundary layer. If the width of the viscous sublayer is much smaller than the width of the inertial sublayer, the gain is not large enough to balance the loss: it is "the vorticity crisis." This leads to the separation of the current and the formation of a northern recirculation gyre (Özgökmen, Chassignet, and Paiva 1997; Kiss 2002).

The 20–25 Sv mean transport associated with the separated currents at 60° W (both layers are taken into account) is compatible with the theoretical estimates based on Sverdrup balance. It also compares with the mean barotropic transport—approximately 20–30 Sv between 65° W and 60° W—obtained by Bryan, Hecht, and Smith (2007) with the Parallel Ocean Program model when the resolution is 0.2°. It is much weaker than the real Gulf Stream transport or the transport modeled by eddy-resolving models (resolution better than 0.1°). This could be explained by the lack of a strong inertial recirculation to the south of the separated western boundary current. Note also that the presence of an overturning

component, similar to the one introduced in the overturning experiment, seems to have no impact on the transport.

In the northern part of the basin, a southward current is found along the western coast (Fig. 4, bottom). It transports approximately 5 Sv at 52° N, a value compatible with the Sverdrup balance but much lower than the observations, because the basin is closed at 55° N and the meridional overturning circulation is not represented. This southward current veers eastward at 49° N, then spreads out southward, and lastly connects to a westward current located at 44° N that forms the northern branch of the northern recirculation area. This branch follows the coastline and meets the separated western boundary current at 40° N. Such a pattern seems compatible with observations and numerical experiments; for example, Bryan, Hecht, and Smith (2007) noticed a complex circulation east of Flemish Cap (with meandering and recirculation depending on the details of their numerical experiments).

The eastward deflection of the southward boundary current near 49° N is a robust characteristic of the model. It is still observed in the stationary and overturning experiments. At this latitude, the first layer has vanished and the second layer is submitted to the direct forcing of the wind stress. The region of negative wind stress curl centered at 45° N, 50° W (see Fig. 1) could then lead to the deflection of the current.

The seasonal variations of h_1 and h_2 remain moderate in the area of the separated western boundary current and scarcely exceed 20 m along its path (see Fig. 3, middle panel). These variations are associated with a meridional shift of the current of approximately 0.2°. In contrast, the separation point experiences larger latitudinal shifts of approximately 1°.

A weak seasonal signal (not shown) is also found on the mass transports of the separated currents: for example, the mass transport at 60° W in the first layer is slightly increased (by approximately 0.1 Sv) from January to August, which agrees with Halkin and Rossby (1985) or Kelly, Singh, and Huang (1999). This represents less than 2% of the total transport associated with the separated current in the first layer.

In the northwestern part of the basin where the second layer outcrops, variations of h_2 of approximately 50 m occur along the coast around 50° N (not shown). In the subtropical gyre, the seasonal cycle is more pronounced than everywhere else. However, the variations of h_1 do not exceed 50 m; opposite variations of h_2 are observed with in general a larger amplitude. A wavelike pattern, more visible in the second layer, has developed in the southeastern corner of the domain. The wavelength is approximately 600–700 km (in the zonal direction), and the meridional extension does not exceed 1,000 km. This signal originates in a region around 20° W and 20° N, where the variations of the wind stress curl are strong (see Fig. 1). Note that a part of this region (east of a line going from 17° W, 21° N to 10° W, 30° N) is over Africa, which explains this particular pattern of the wind stress. The signal vanishes when a steady wind forcing is applied, as in the stationary experiment (see Fig. 5, top panel). Consequently, it is the signature of Rossby waves forced by a periodic signal in a closed basin, whose the theory can be found, for example, in LaCasce (1980).

Note that Kelvin waves propagated along the coastlines and Rossby waves radiated from the eastern boundary during the spin-up. The propagation of Kelvin waves was no longer

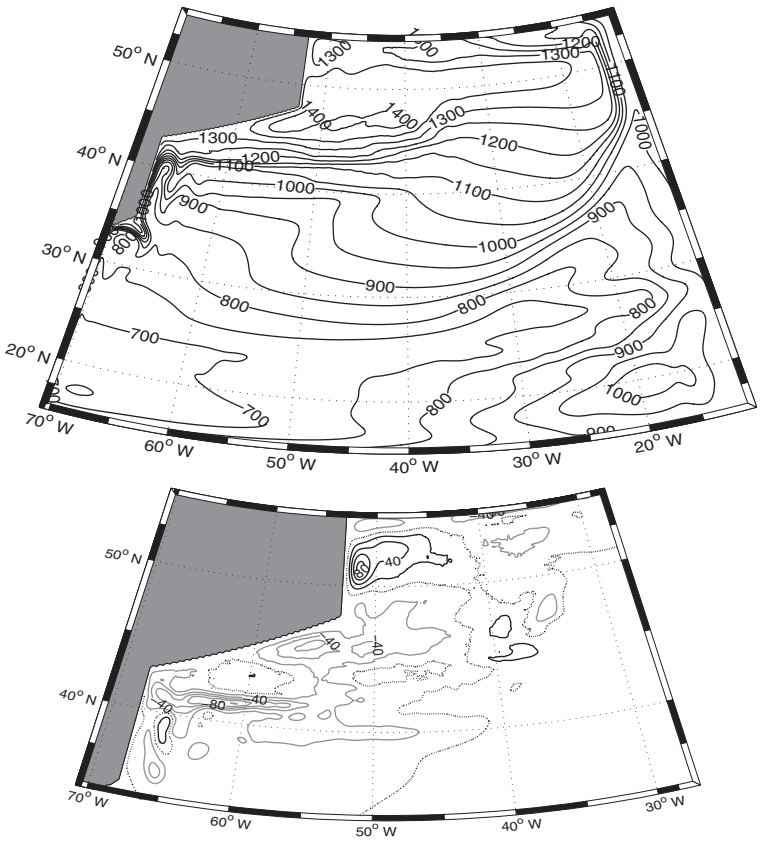

Figure 5. January mean of the second-layer thickness h_2 (top) for the stationary experiment. Differences between the January means of h_2 (bottom) obtained from the stationary experiment and the reference experiment. The means have been computed from the last 120 years of the experiments (units: m).

seen when the model reached a quasi-equilibrium state. The wavelike pattern, therefore, cannot be linked to such a propagation.

b. The stationary experiment

In the experiment with a steady wind stress, the ocean response does not display seasonal variations any longer. However, the obtained mean state shows only small differences with the obtained one in the reference experiment.

The separated western boundary current is shifted northward of approximately 0.25°–0.50°, with a corresponding decrease of the outcrop area. In the northwestern part of the basin, in the area where the second layer outcrops and where the seasonal variation of the

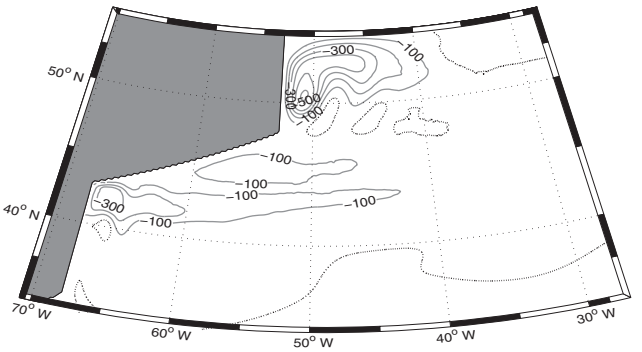

Figure 6. Differences between the January means of h_2 obtained from the overturning experiment and the reference experiment. The means have been computed from the last 120 years of the experiments (units: m).

wind is strong, an increase of the second-layer thickness of approximately 50 m is also observed (see Fig. 5).

The causes of the moderate shift of the separated current are not clear. The vanishing of the wavelike pattern in the subtropical gyre and the changes in the outcrop area close to the windswept shores of the Labrador may have an impact on the ocean dynamics at the basin scale and induce the small changes observed on the position of the separated current.

c. The overturning experiment

The changes are more important when a meridional overturning circulation is introduced in the model (see Section 2b for the details of the setup). The cyclonic circulation in the northern gyre is intensified around the region where the downward flux is prescribed (see Fig. 6) and gives rise to an increase of approximately 20 Sv in the transport of the southward current, which flows along the coast at 53° W. On the other hand, the size of the northern recirculation gyre has been reduced, and the current has shifted northward of approximately 2° in comparison with the reference experiment. However, the mean transport along the northern coast at 60° W or the mean transport in the separated western boundary current remains practically unchanged.

A southward shift of the separated current has been frequently found in numerical simulations of the Atlantic Ocean (see, for example, Gerdes and Köberle 1995; Spall 1996a, 1996b). More recently, a northward shift has been also observed in de Coëtlogon et al. (2006), Kwon et al. (2010), or Kwon and Frankignoul (2012). De Coëtlogon et al. (2006) suggested that such a shift could be explained either "by the inherent coupling between the thermohaline and the wind driven circulation" or by "the North Atlantic Oscillation variability driving them on similar time scales in the models" (p. 2119). In Section 5 of

their review paper, Kwon et al. (2010) also listed several candidates that might control the position of the Gulf Stream (the wind stress, the cooling or warming of the subpolar gyre that intensifies or inhibits the convection, and the bottom torque associated with the deep western boundary current west of the Grand Banks) but concluded that it was difficult to establish "which mechanisms primarily control the Gulf Stream shifts and how they are related to the AMOC [Atlantic Meridional Overturning Circulation]." (p. 3273)

Here, no bottom torque is applied and the wind stress is unchanged. We thus have to examine a less difficult problem—namely, how an ad hoc overturning circulation may act on the Gulf Stream. To investigate this link, we first consider the model described by equations (1) and (2) in a stationary state. Outside the western boundary currents (a few degrees east of the western boundary), the equations for the meridional momentum can be simplified by neglecting the advection and diffusion terms (Sverdrup balance). This leads to the relations

$$f h_1 u_1 = -h_1 \partial_y (2bh_1 + bh_2) + \tau_{0,y} - \tau_{1,y} \quad \text{and}$$
$$f h_2 u_2 = -h_2 \partial_y (bh_1 + bh_2) + \tau_{1,y}.$$

Adding these two equations, we obtain

$$f \Phi_z = -\partial_y [(bh_1^2 + bH^2)/2] + \tau_{0,y}, \tag{3}$$

where $H = h_1 + h_2$ and Φ_z is the zonal mass flux $h_1 u_1 + h_2 u_2$.

Subscripts r and o will be used subsequently to distinguish the reference experiment from the overturning one. To compare more easily the mean solutions of both experiments, we form the differences $h_{1,o} - h_{1,r} = \delta h_1$, $H_o - H_r = \delta H$, and $\Phi_{z,o} - \Phi_{z,r} = \delta \Phi_z$ and assume that they remain small in order to linearize the equations they verify. As the wind stress remains unchanged in both experiments, equation (3) implies that

$$f \delta \Phi_z = -\partial_y (bh_{1,r} \delta h_1 + bH_r \delta H)$$

The zonal transport (in particular that associated with the separated western boundary current) remains nearly unchanged for both experiments; hence, $\delta \Phi_z \simeq 0$ and $h_{1,r} \delta h_1 + H_r \delta H$ is a function of x alone. However, because the meridional velocity vanishes at the southern boundary, the Sverdrup balance implies $\partial_x (h_{1,r} \delta h_1 + H_r \delta H) = 0$ along this boundary, and consequently, $h_{1,r} \delta h_1 + H_r \delta H$ remains unchanged. On the other hand, w_e is positive everywhere except for the northernmost part of the basin. This implies that $\delta H > 0$ (the total thickness must increase in the southern part of the basin because some water is removed from the northern part and introduced there). Consequently, $\delta h_1 < 0$. As the total volume of water in the first layer is also unchanged, a global decrease of h_1 induces an expansion of the area covered by the first layer and, therefore, a northward shift of the outcrop line. This analysis thus explains how an increase in the meridional overturning associated with no variations of the zonal mass transport leads to a northward shift of the separated western boundary current.

We now examine if the zonal mass transport can remain unchanged. Let us note the meridional mass transport $\Phi_m = h_1 v_1 + h_2 v_2$. The zonal transport is linked to the meridional transport through the mass conservation equation. The differences between the mass transports of the overturning and reference experiments thus verify

$$\partial_x \delta\Phi_z + \partial_y \delta\Phi_m = w_e.$$

Because w_e does not depend on x, a possible solution is given by $\delta\Phi_z = 0$ and $\delta\Phi_m = \int w_e dy$: in the overturning experiment, the zonal transport remains unchanged, but a northward anomaly of the meridional transport emerges, its maximum being reached along the latitude where w_e vanishes.

In conclusion, the stationary response of the model in the overturning experiment is characterized by a nearly unchanged zonal mass flux in comparison with the reference experiment and, consequently, a more northward separated western boundary current. Our analysis suggests that this response is linked to the simplicity of the setup we have adopted: the velocity w_e does not depend on the zonal direction in the largest part of the basin. It is probable that a more complex setup (including the effect of a topography or modeling a more realistic overturning) would lead to variations of the zonal transport and, consequently, a different shift of the separated western boundary current.

This analysis differs from but does not contradict the one made by Kwon and Frankignoul (2014) about the shifts of the Gulf Stream. They argue that a southern shift of the Gulf Stream is observed only if the crossover between the deep western boundary current and the Gulf Stream occurs close to the western boundary, in the Slope Water region, where the bottom torque is large. This process is not represented in our model and thus cannot induce a southern shift. In low-resolution models, they associate a northward shift of the Gulf Stream to a crossover between the deep and surface currents above the mid-Atlantic ridge, leading to an opposite bottom torque. This mechanism cannot occur in our experiments. The global constraints that are applied on the two layers (they keep the same volume) associated with a uniform injection of water under the southern gyre suffice to explain this behavior.

4. Interannual variability

We emphasize again that interannual variability here means the ocean variability along the outcrop line when the ocean is forced by a wind that only contains the climatological seasonal cycle.

a. The reference experiment

The path of the strongest branch of the separated western boundary current can be estimated from the position of the isolines of h_1 close to the outcrop line. As an illustration, the monthly means of the 300 m isolines of h_1 are shown in Figure 7 for the 25th and 31st years of the reference experiment. During the 25th year, only small lateral shifts, which

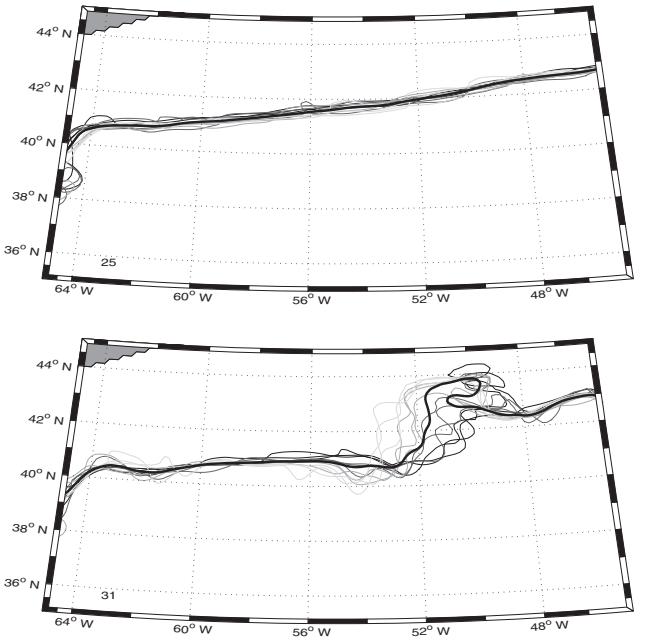

Figure 7. Monthly paths of the Gulf Stream estimated from the isoline $h_1 = 300$ m for the 25th year of integration (top) and the 31st year (bottom). The corresponding mean path is indicated by the thick line.

scarcely exceed 30 km, affect the path of the current from the separation point up to 2,000 km westward. By contrast, during the 31st year, a meander has formed around 52° W: in consequence, the mean path undergoes a southward shift of 0.5° at 60° W and of 1° at 56° W but a northward shift larger than 1° at 50° W. This suggests that the interannual variations are larger than the seasonal ones. This is verified by means of a PC analysis (Fig. 8) made on the 120 annual means of h_1 over the represented domain.

In this figure, the grayed-out surface (light gray) corresponds to the outcrop area: there, the first layer has vanished at least once during the time integration. The first and second EOFs, which represent respectively 17.8% and 14.0% of the total variance, show a succession of highs and lows along the outcrop line. The associated PCs are in quadrature: the correlation between the first two PCs is maximal when the lag is between 3 and 4 years and exceeds 0.6; it is significant (threshold value of 0.2). A significant peak appears at approximately 15 years when a spectral analysis is done (not shown). These results suggest the existence of westward propagating waves with a dominant period of approximately 15 years. This propagation is obvious in the Hovmöller diagram of Figure 9. The wave front is strongly marked as shown by the rapid variations from blue to red ahead of the wave. Behind the front, the anomalies generally remain large (they exceed 400 m) over several degrees of latitude, then decay up to approximately 0–50 m. The PC analysis (particularly the highs

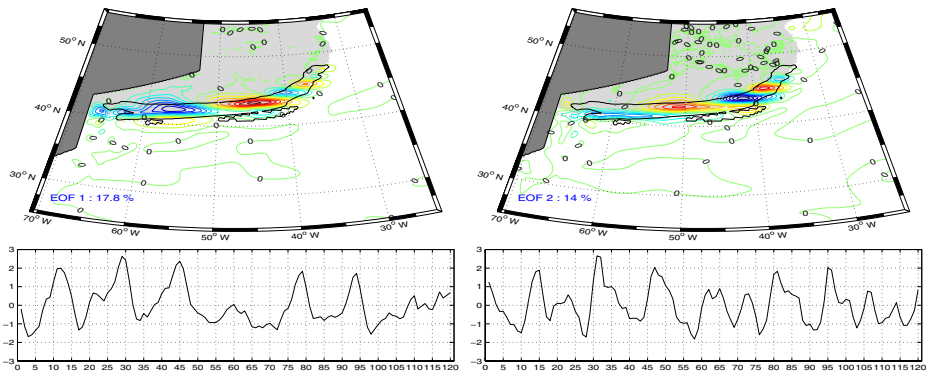

Figure 8. First and second EOFs (contour interval: 10 m) of the first-layer thickness with the corresponding normalized PCs. The analysis is performed on the annual means of the last 120 years of the reference run, and the grayed-out surfaces show the outcrop area. The black bold contour delineates the area where the relative difference between the meridional gradients of h_1 and $2h_1 + h_2$ is smaller than 10%. EOF, empirical orthogonal function; PC, principal component.

and lows of the EOFs, which become more elongated during the propagation), as well as this Hovmöller diagram, suggests that a nonlinear mechanism drives the propagation of these waves (see Section 5).

The previous results are robust; they remain nearly unchanged (only the details of the pattern of the EOFs or the percentage of variance are slightly modified) when the analysis is performed on the whole domain or with a monthly time series.

This low-frequency variability is also found when the analyses are done on the second-layer thickness or the mass transports. For example, Figure 10 shows the EOFs and PCs of the mass transport in the first layer across the meridian 60° W between 32° N and 44° N computed from the monthly time series. The first and second EOFs represent respectively 33.4% and 24.6% of the total variance, and the variability of the resulting PCs is dominated by low frequencies. When a 1-year low-pass filter is applied on the PCs, the resulting time series (thick line) are significantly correlated with the PCs of h_1 or h_2 and show the same spectral properties. For example, the correlation between the first PCs of the transport and h_1 is -0.8 when the transport leads h_1 with a time lag of 3 years.

b. The stationary experiment

The results concerning the first layer are essentially the same when the wind stress is stationary. The first two EOFs of h_1 contain, however, a slightly smaller part of the total variability. The changes are more important in the second layer: the response is now dominated by waves—the period is approximately 5 years, and the wavelength approximately 400 km—which propagate from around (38° W, 45° N) toward the northwestern part of the basin. These waves appear on the first two EOFs of h_2, which represent 21% of the total

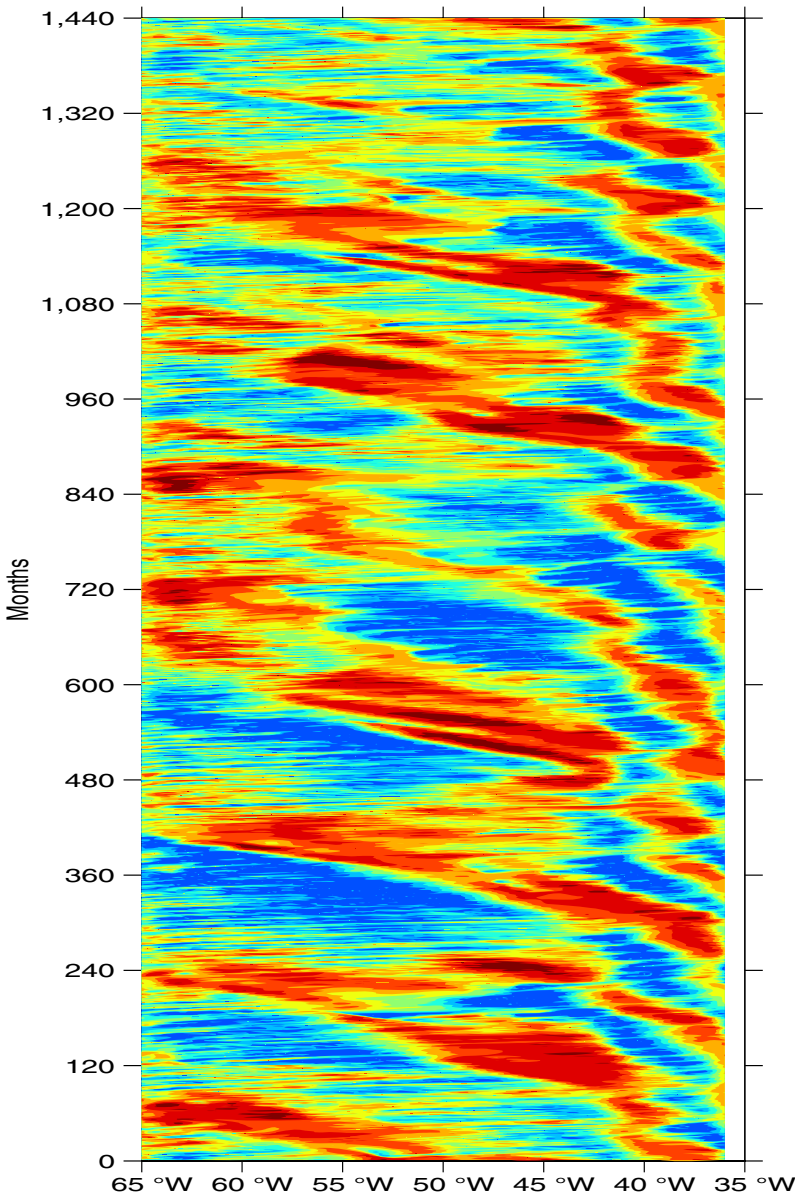

Figure 9. Hovmöller diagram (abscissa: longitude; ordinate: time in months) of the first-layer thickness along the mean path of the separated western boundary current. The values range from 0 m (dark blue) to 400 m (dark red). The mean path has been computed from the position of the 200 m isoline.

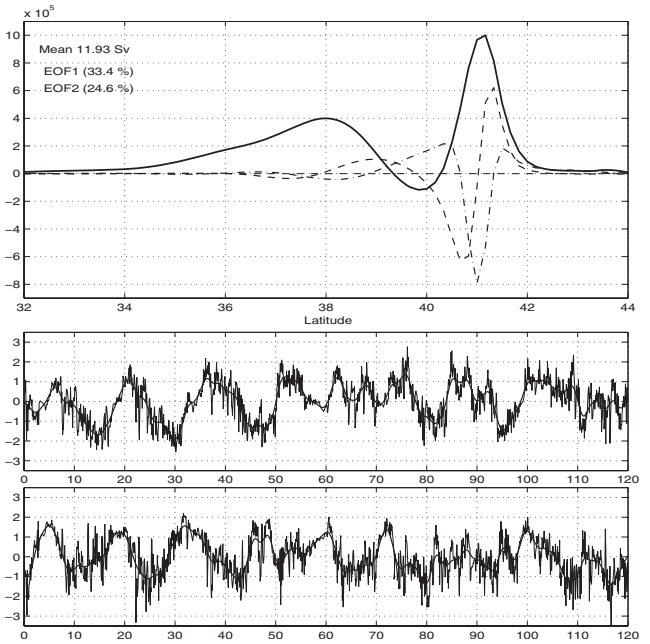

Figure 10. First (dashed line) and second (dash-dotted line) EOFs and corresponding PCs (gray lines in the lower panels) of the monthly zonal transport at 60° W between 32° and 44° N for the first layer (units: $m^3\ s^{-1}$). The thick black line in the upper panel shows the mean value of the zonal transport at 60° W. The thick black lines in the lower panels have been obtained by filtering the periods shorter than 1 year. EOF, empirical orthogonal function; PC, principal component.

variance (the first EOF and PC are shown in Fig. 11). The pattern is reminiscent of the basin modes observed in simple models (see, for example, Cessi and Louazel 2001). In the reference experiment, the seasonal variability may enhance the variability along the separated western boundary current and prevent this mode from being immediately detected. This would agree with Sirven et al. (2007) who showed that a stochastic forcing does not efficiently excite basin modes. The low-frequency waves that propagate along the outcrop line are represented on the third and fourth EOFs of h_2 (not shown). They contain approximately 16% of the total variance (8% each).

c. The overturning experiment

In the overturning experiment, the first EOF of h_1 (Fig. 12) resembles the one obtained in the reference experiment. On the contrary, the second EOF (not shown) shows large differences in the western part of the basin with the second EOF of the reference experiment, and its PC is no longer significantly correlated with the PC of the first EOF. This shows that the westward propagation of waves along the outcrop line is altered. However, when the PC

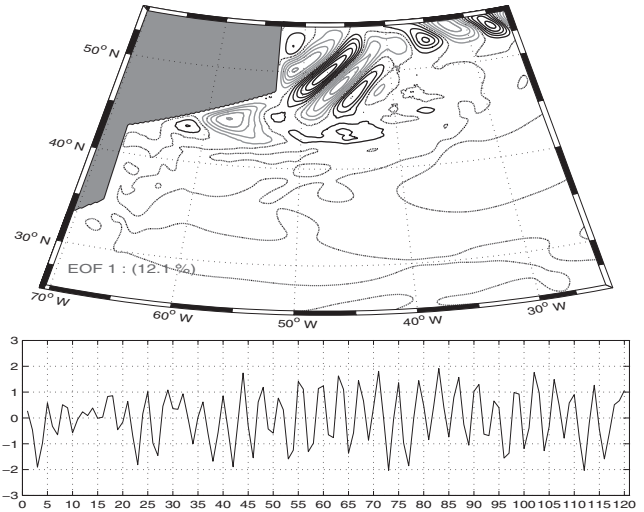

Figure 11. First EOF (contour interval: 10 m) and corresponding PC of the second-layer thickness for the stationary experiment. The analysis is performed on the last 120 annual means of the run. EOF, empirical orthogonal function; PC, principal component.

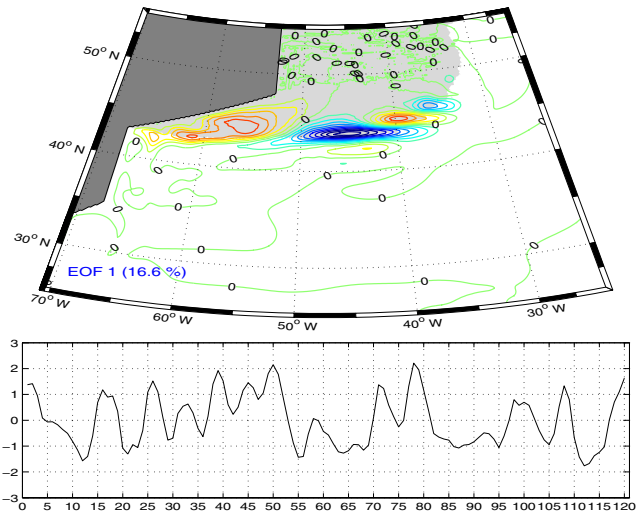

Figure 12. First EOF (contour interval: 10 m) and corresponding PC of the first-layer thickness for the overturning experiment. The analysis is performed on the last 120 annual means of the run, and the grayed-out surface shows the outcrop area. EOF, empirical orthogonal function; PC, principal component.

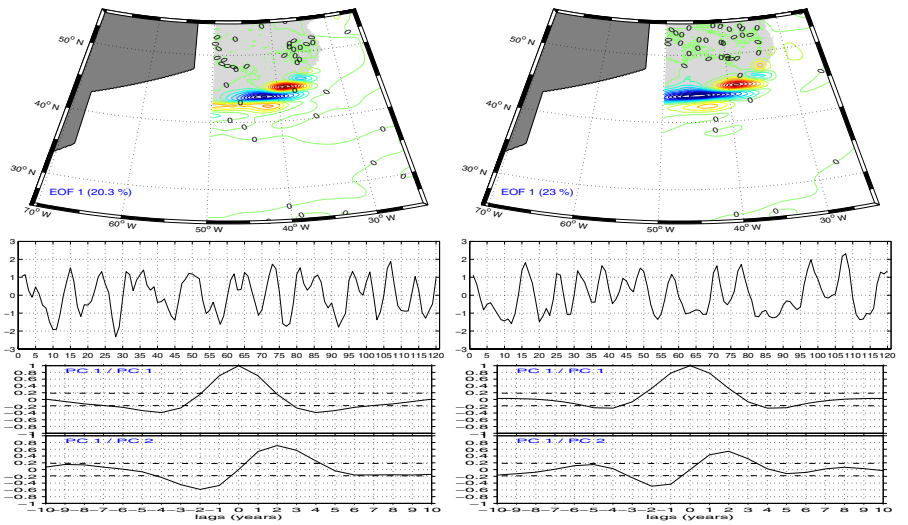

Figure 13. First EOF (contour interval: 10 m) and corresponding PC of the first-layer thickness for the reference experiment for the eastern part of the basin (left). The autocorrelation of the first PC and the correlation between the first and second PCs are shown just below. The significance level is indicated by the dash-dotted line. Similar figures for the overturning experiment (right). The analysis is performed on the last 120 annual means of the runs, and the grayed-out surfaces show the outcrop areas. EOF, empirical orthogonal function; PC, principal component.

analysis is performed on a reduced domain (see Fig. 13), the results become very similar in both experiments. The first two EOFs are almost identical (it is the same thing for the second EOFs, which are not shown), and the lag between the PCs shows that the pattern propagates westward as expected. Note that the dominant timescale is now reduced to 8 years (it was approximately 15 years in the reference experiment). The model presented in the next section will clarify this point.

The waves, which originate in an area centered around 36° W, 46° N and propagate westward along the outcrop line, whatever the experiments, are a characteristic feature of the model. Their EOFs, however, represent a smaller percentage of variance in the stationary experiment, and they cannot reach the western coast in the overturning experiment because the mean state has changed. The mechanism driving these waves is now presented.

5. A simple model of the propagating waves

In this section, we develop a simple analytical model, which qualitatively explains the dynamics of the outcrop line. We first consider a case where the forcing and dissipation

are negligible, then briefly examine how the results are modified when they are taken into account. As this model presents some similarities with those used in thin-jet theory (Cushman-Roisin, Pratt, and Ralph 1993; Sasaki and Schneider 2011a), we mention subsequently some analogies and differences between the two approaches.

To facilitate the analytical computations, a new system of coordinates (X, Y), with X and Y respectively along and across the front, is defined. The length scale along the front ($\simeq$1,000 km) is much larger than that across the front ($\simeq$50 km), whereas the component of the velocity along the front U ($\simeq$0.2 m s^{-1}) is much larger than the component across the front V. Consequently, the velocity along the front can be estimated by geostrophy,

$$fU = -\partial_Y[b(2h_1 + h_2)],$$

and the relative vorticity $\zeta = \partial_X V - \partial_Y U$ is approximatively equal to $-\partial_Y U$.

The momentum equation along the X axis allows us to estimate the velocity across the front V. As only low-frequency variability (annual to decadal timescale) is considered, the term $\partial_t U$ can be neglected. The equation thus reads

$$U\partial_X U + V\partial_Y U - fV = -\partial_X[b(2h_1 + h_2)]$$

or, equivalently,

$$(-\partial_Y U + f)V = \partial_X[b(2h_1 + h_2)] + U\partial_X U.$$

In the considered domain, the relative vorticity $\zeta \simeq -\partial_Y U$ is negligible in comparison with the planetary vorticity; indeed, we have $f \simeq 10^{-4}$ s^{-1} and $|\partial_Y U| \leq 0.2$ m s^{-1}/50 km $< 10^{-5}$ s^{-1}. In conclusion, the component of the velocity across the front is only computed from the gradient of the Bernouilli function $[b(2h_1 + h_2)] + U^2/2$:

$$fV = \partial_X[b(2h_1 + h_2)] + U\partial_X U.$$

The gradients of h_1 and $2h_1 + h_2$ have been computed. In Figure 8, over the surface limited by the black bold curve, the relative difference between the meridional gradient of h_1 and that of $2h_1 + h_2$ remains smaller than 10% (similar results are obtained for the zonal gradient). This domain coincides with the area where the waves propagate. Consequently, the gradient of $2h_1 + h_2$ is approximated by that of h_1 alone in the previous two equations, which yields:

$$fU = -\partial_Y(bh_1) \quad \text{and} \quad fV = \partial_X(bh_1) + U\partial_X U.$$

These equations, completed by the mass conservation equation, enable the determination of h_1.

The hypotheses made by Sasaki and Schneider (2011a) or more generally in thin-jet theory are close to those made here. First, these authors use an equivalent barotropic model.

Here, such a model has been obtained by replacing the gradient of $2h_1 + h_2$ with that of h_1. Secondly, they neglect the time derivatives of U, V, and h_1 (low-frequency variability). Here we keep the term $\partial_t h_1$ and we explain subsequently why this term is important. On the contrary, the relative vorticity is neglected in comparison with the absolute vorticity, an approximation that is not done in thin-jet theory.

The expressions of U and V are now introduced in the mass conservation equation, which yields after simplifications:

$$\partial_t h_1 - \frac{bh_1}{f^2}(-\partial_X f\, \partial_Y h_1 + \partial_Y f\, \partial_X h_1) + \partial_Y \left[\frac{b^2 h_1}{f^3}(\partial_Y h_1)(\partial_{XY} h_1) \right] = 0. \tag{4}$$

The long Rossby wave term $\frac{bh_1}{f^2}(-\partial_X f\, \partial_Y h_1 + \partial_Y f\, \partial_X h_1)$ is comparable to or larger than the third term in this equation when h_1 is large. However, as it is proportionnal to h_1, it vanishes with the first-layer thickness. In this case, the third term becomes dominant because it contains $\frac{b^2}{f^3}(\partial_Y h_1)^2 \partial_{XY} h_1$ proportional to the only derivatives of h_1.

Note that $\partial_t h_1$ does not vanish along the outcrop line, although h_1 vanishes. To prove this, let us note $Y = Y_f(X, t)$ the position of the front; this definition implies that $h_1(X, Y_f(X, t), t) = 0$ for all X and t. Consequently, the differential of h_1 along the outcrop line also vanishes: $dh_1 = 0$. On the other hand, $dh_1 = \partial_X h_1 dX + \partial_Y h_1 dY + \partial_t h_1 dt$. From these last two relations, we deduce that for a fixed value of X along the outcrop line, h_1 verifies

$$\partial_t h_1 + \partial_Y h_1 dY_f/dt = 0.$$

Along the outcrop line, $\partial_Y h_1$ does not vanish. As shown in Figure 14, in the vicinity of the outcrop line, this term is even very large. The term dY_f/dt represents the meridional velocity of the outcrop line. As the latter moves, this second term also does not vanish. Consequently, we cannot assume that $\partial_t h_1$ vanishes. This computation also shows that this term in this simplified model permits us to take into account the shifts of the outcrop line.

Finally, in a narrow strip close to the outcrop line (less than approximately 100 km), the evolution of the first-layer thickness is given by

$$\partial_t h_1 + \partial_Y \left[\frac{b^2 h_1}{f^3}(\partial_Y h_1)(\partial_{XY} h_1) \right] = 0. \tag{5}$$

It simply expresses a balance between the fluctuations of thickness close to the front and the mass fluxes perpendicular to the front, caused by the *ageostrophic part of the current*. Note that the ageostrophic part of the current also plays a prominent role in thin-jet theory.

As the separated current is nearly zonal, we can neglect the partial derivative $\partial_X f$, which is much smaller than $\partial_Y f \simeq \beta$. In this case, equation (5) admits solutions that can be found by

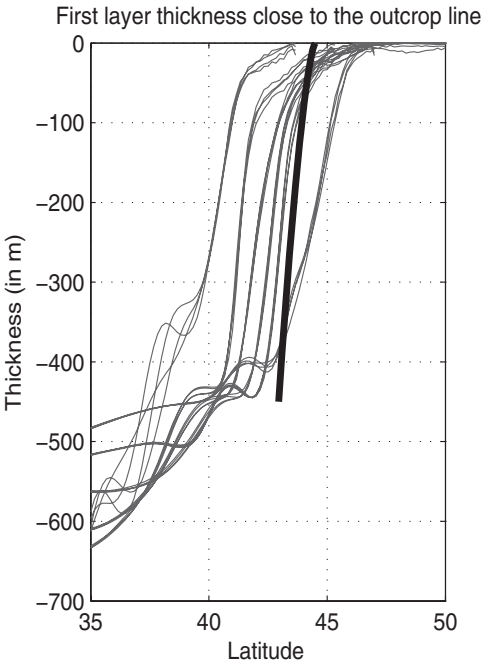

Figure 14. Mean profiles of h_1 at 45°, 50°, 55°, 60°, and 65° W in January, April, July, and October (thin gray lines) and profile (thick line) given by the theoretical model.

separating the variables. Indeed, looking for solutions such as $h_1(X, Y, t) = P(X, t)H(Y)$, it is transformed in a system of two equations:

$$\begin{cases} \mathcal{A}H + \partial_Y[(b^2/f^3)H(\partial_Y H)^2] = 0 \\ \partial_t P - \mathcal{A}P^2\partial_X P = 0, \end{cases} \tag{6}$$

where $\mathcal{A}$ is an arbitrary constant, which characterizes the propagation velocity of the waves (second equation in 6).

The first equation in (6) allows us to predict qualitatively the profile of the front south of the line $Y = Y_0$ close to the outcrop line. It can be numerically solved when f depends on Y (e.g., $f = f_0 + \beta Y$). It is, however, interesting to solve it analytically for a constant f because this enlightens a crucial property of the constant $\mathcal{A}$. If f is constant, this equation becomes $\mathcal{A}H/(fL^2) + H'^3 + 2HH'H'' = 0$ where $L = b/f^2$ is equal to 400 km ($b = 0.004$ m s^{-2} and $f = 10^{-4}$ s^{-1}). It is then integrated in

$$H^{3/2}H'^3 + \mathcal{A}(3H^{5/2} + 2H_s^{5/2})/(5fL^2) = 0,$$

where H_s is an arbitrary constant. A second integration from the outcrop line leads to the solution

$$Y_0 - Y = \frac{3}{2}(5fL^2H^2/3\mathcal{A})^{1/3} \tag{7}$$

when H_s is equal to 0, and to the solution

$$Y_0 - Y = (5fL^2H_s^2/\mathcal{A})^{1/3} \int_0^{H/H_s} \frac{dx}{(3x + 2x^{-3/2})^{1/3}} \tag{8}$$

when H_s differs from 0. Because these solutions are only valid south of the outcrop line ($Y \leq Y_0$), the arbitrary constant $\mathcal{A}$ must be positive.

A typical profile obtained from the analytical solution (7) is shown in Figure 14 for $\mathcal{A} = 650$ km y^{-1} and compared with the profiles observed in the reference experiment between 45° W and 65° W ($\mathcal{A}$ has been estimated from Fig. 9). The agreement between the theoretical and numerical models is good, considering the simplicity of the theoretical model.

In a close vicinity of the outcrop line, H is proportional to $(Y_0 - Y)^{3/2}$ when H_s is equal to 0 (solution shown in Fig. 14), and to $(Y_0 - Y)^{2/3}$ when H_s is different from 0. The first solution is closer to the numerical results. However, the solutions computed from equation (8) ($H_s \neq 0$) remain very similar to the solution shown in Figure 14, except that they give a steepest profile, because the slope at $Y = Y_0$ becomes infinite. They are compatible with the numerical results when H_s remains smaller than approximately 300 m. In this case, H_s gives a typical depth over which the front remains nearly vertical.

The second equation in (6) characterizes the wave behavior of the solution.[1] It can be solved by the method of characteristics: P remains constant equal to P_0 on the straight lines of equation $X = -\mathcal{A}P_0^2 t + X_0$. The propagation velocity is always negative because $\mathcal{A}$ is positive, which corresponds to a westward propagation. This agrees with Figures 8 and 9.

An analytical solution of this equation is shown in Figure 15(a) to illustrate the properties of the waves. A constant anomaly is prescribed at $t = 0$, $X = 0$ and is suppressed after a time, T_0. The position of the wave front has been computed using the Rankine-Hugoniot condition (this means that the front velocity is equal to $[\mathcal{A}P^3/3]/[P]$, where the brackets [ ] denote the jump of P or P^3 across the front). There is no propagation at the rear of the anomaly because h vanishes, a choice that is not very realistic but allows an analytical computation.

The deformation of the wave associated with the nonlinear nature of the wave equation shows that there is a transfer of energy from small spatial scales to larger ones. This transfer goes with a decrease of the amplitude of the head front as the anomaly travels westward. In the example shown in Figure 15(a) the amplitude of the head front is divided by 2 at

1. This equation has the same form as the equation characterizing the creeping of a paint patch on a wall under the effect of the gravity.

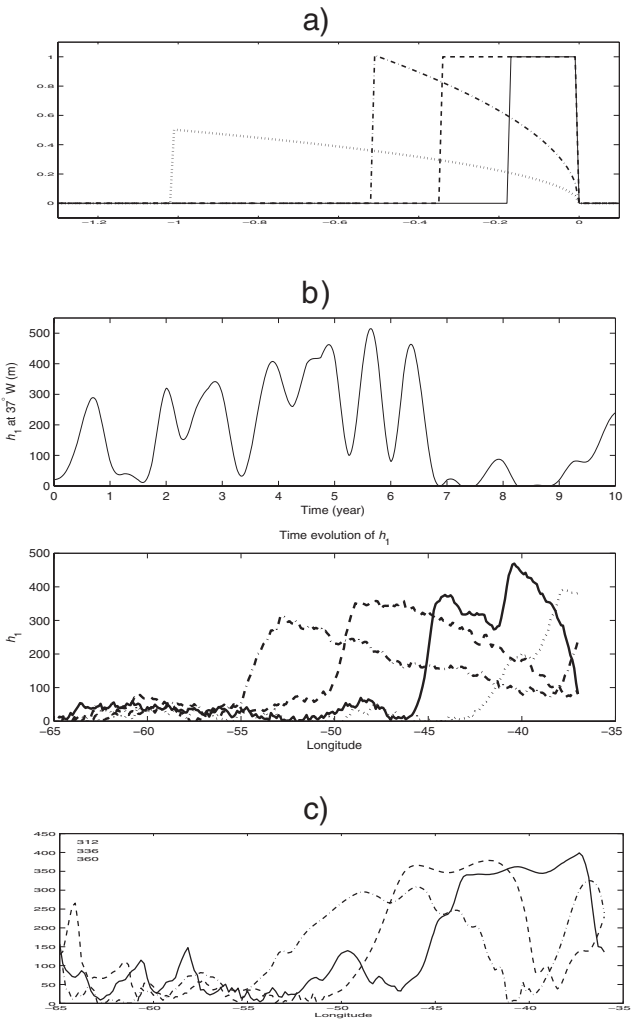

Figure 15. (a) Response of the analytical model to a constant anomaly, P_0, prescribed at $x = 0$ between $t = 0$ and $T = T_0$. The response is shown at $T_0/2$ (thick line), T_0 (dashed line), $3T_0/2$ (dash-dotted line), and $5T_0$ (dotted line). The horizontal and vertical axes represent $X/(\mathcal{A}P_0^2T_0)$ and P/P_0. (b) An anomaly is prescribed at $x = 37°$ W during 10 years. The resulting propagating pattern (units: m), as predicted by equation (9), is shown at $t = 24$ (dotted), 48 (solid), 72 (dashed), and 96 (dash-dotted) months. (c) Example of a westward propagation along the outcrop line in the reference experiment (h_1 is shown for the months 312, 336, and 360).

a distance equal to $\mathcal{A}P_0^2T_0/3$ from the source. With $\mathcal{A} = 650$ km y^{-1} and $P_0 = 1$, the anomaly is attenuated by a factor of 2 at 217 km from its source when the process of formation takes 1 year, and at 3,250 km when it takes 15 years. Consequently, only the low-frequency anomalies may cross the basin with an amplitude that is large enough to permit their observation.

To compare in a more precise way the solutions of the wave equation and the waves shown in Figure 9, we have numerically integrated the equation

$$\partial_t P - \mathcal{A}P^2\partial_X P = \nu\partial_{XX}P + \Omega. \tag{9}$$

The viscous term $\nu\partial_{XX}$ has been added to facilitate the numerical computation. We can thus avoid employing the tricky methods that directly compute the position of the wave front. Moreover, it adds a small dissipation that is present in the model. Ω is a white noise that helps represent the errors associated with the model as a random process. Both terms are much smaller than the terms on the left-hand side of the equation. In the area where the waves arise, h_1 varies because of the forcing and the interior ocean dynamics. These variations are introduced as a boundary condition at $X = 37°$ W. The time series shown in Figure 15(b), gives an example of such a boundary condition. It has a white spectrum for a period ranging between 1 and 4 years. The corresponding solution obtained for $\mathcal{A} = 650$ km y^{-1} is shown just below. It is in qualitative agreement with the propagating waves observed in the reference experiment after the 312th month of integration (Fig. 15**c**). The waves propagate westward. The initial pattern is nearly not deformed during the first months of the propagation; the amplitude of the anomaly decreases afterward, and the basis of the anomaly becomes wider.

The system of equations in 6 predicts waves that propagate westward, although the long Rossby wave term has been neglected. This direction of propagation is associated with the fact that the water in which the wave propagates is located to the south of the outcrop line in the Northern Hemisphere (see equation 8). The propagation would be eastward in the opposite case, where denser water would outcrop to the south of lighter water.

When h_1 increases (or, equivalently, the distance to the outcrop line increases), the long Rossby waves have theoretically to be taken into account (see equation 4). We detected long Rossby waves across the basin—with characteristics consistent with the theory: the phase velocity increases toward the equator and its value is in agreement with the theory for a 2.5-layer model—only during the spin-up. However, afterward these waves were no longer seen, and the statistical analyses that we tried to detect them failed for the three experiments.

We have obtained equation (4) and studied its properties when the viscosity vanishes and the forcing is negligible. The first hypothesis is not verified in the numerical experiments because the viscosity is equal to 400 m^2 s^{-1}. However, the impact of this term is easily guessed: it smoothes the pattern of the solutions and suppresses the discontinuities. This has been verified by the numerical computation of equation (9). Similarly, the impact of the forcing term, introduced as a white noise in equation (9), is easy to describe: The variable P

is no longer conserved along the characteristics but suffers changes caused by the forcing. When the latter remains small, the changes remain also small as verified by integrating equation (9).

6. Conclusion

This study investigates the dynamics of a separated western boundary current using a reduced-gravity 2.5-layer model with simple coastlines, which reproduce in a simplified way the geometry of the North Atlantic (between 70° W and 10° W and 15° N and 55° N). In this model, the second layer outcrops in the northern part of the basin, which constitutes an original feature in comparison with most of the idealized studies.

The model is driven by a realistic seasonal wind stress in the reference experiment. Two additional experiments were made: in the stationary experiment, a steady wind stress is used, and in the overturning experiment, mass fluxes are prescribed at the basis of the second layer in order to represent a meridional overturning circulation. In all the experiments, the obtained mean state shows a separated western boundary current, with, to its north, a complex recirculation gyre. However, the separated western boundary current is shifted northward by approximately 2°, and its mass transport is slightly increased when the meridional overturning circulation is added. The dynamics in the northern recirculation gyre are also modified, but the changes remain moderate, considering the large increase of the mass transport (approximately four times greater than in the reference experiment), which occurs more northerly along the coast.

The mean seasonal signal along the path of the separated current remains weak and is compatible with the results of Kelly, Singh and Huang (1999). In all the experiments, the variability is much stronger at interannual periods. It is characterized by westward propagating patterns along the outcrop line, whose dynamics are strongly nonlinear. However, in the stationary experiment, the EOFs that describe them represent a smaller percentage of variance, probably because the steady forcing does not bring enough energy to excite them in the area where they arise.

A preferred timescale of approximately 15 years is observed when no attempt to represent the meridional overturning circulation is done; it is replaced by a timescale of approximately 8 years when the latter is modeled. The timescale depends on the mean state and, more widely, on the setup of the model (size of the domain where the wave can propagate without being distorted, parameterizations, etc.); hence, its significance is weak. On the contrary, the fact that the low frequencies (lower than approximately 0.25 y^{-1}) are preferred in the area of the separated western boundary current is robust because it rests on nonlinear dynamics independent of the model setup.

A simple analytical model has been developed to explain the properties of the response observed in the numerical experiments and to highlight the mechanisms driving the propagation of the nonlinear waves along the outcrop line. It is only valid in close vicinity of the outcrop line. In this model, the fluctuations of the first-layer thickness are nearly balanced

by the mass fluxes due to the ageostrophic part of the current and perpendicular to the front. Their evolution is thus driven by a nonlinear wave equation.

This model allows us to describe the propagation of waves excited by a random forcing around 38° W, 45° N, where the eastern extremity of the outcrop line lies. It predicts a westward propagation with a velocity linked to the meridional gradient of the first-layer thickness. The β effect plays no role in this direction of propagation. Because it is nonlinear, it allows energy transfers from small to large spatial scales and favors low frequencies. A preferred timescale of approximately 15 years (8 years) is thus predicted when the waves can propagate over approximately 3,000 km (1,500 km as in the overturning experiment).

This model differs from the models used in thin-jet theory because the first-layer thickness is allowed to vanish. The waves that are predicted are thus different from those predicted by this theory. In particular, the meandering of the jet cannot be represented in our model. When h_1 becomes large, the long Rossby wave propagation must be taken into account (see equation 4). However, the transition from one type of wave to the other is certainly smooth because both waves have quite similar propagation velocities.

The mechanism described here might explain why the low-frequency variability of the Gulf Stream is easier to detect than the seasonal variability in the observations or the models (see, for example, Frankignoul et al. 2001; Rossby, Flagg, and Donohue 2010). Note, however, that the heat exchanges with the atmosphere in the Gulf Stream area are not represented here and might modify the properties of these waves.

From a more theoretical viewpoint, the results found here obviously do not contradict those coming from the theory of dynamical systems. Only the focus is different. In the dynamical system approach, the properties of the system are explored over a wide range of values that some parameters (e.g., the Froude number) may take. For example, Primeau and Newman (2007) found in a 1.5-layer model a regime in which one of the equilibrium solutions has a large outcropping region. This solution equilibrated to a stable period orbit with a period of 8 months. Shimokawa and Matsuura (2010) similarly showed with a time-dependent forcing but a quasi-geostrophic model that at least two different regimes were possible. Here, no parameters are modified. Our initial choice makes possible the existence of a large outcrop area and of propagating patterns; rather than exploring the bifurcations diagram of the model, we concentrate on the wavelike patterns and their properties.

Similarly, these results do not contradict those of Sirven (2005). He studied the part of the low-frequency variability driven by an external low-frequency forcing and showed how the latter could act close the outcrop line. A case combining these two aspects will be considered in a next paper.

Acknowledgments. We thank Claude Frankignoul and the anonymous reviewers for their comments, which were helpful in improving the manuscript. This work was supported in part by the French Program LEFE/EVE. Some computations have been done at the Institut du Développement et des Ressources en Informatique Scientifique.

APPENDIX

As the second layer may outcrop, the leapfrog scheme with an Asselin filter used in Février, Sirven, and Herbaut (2007) has been modified. A leapfrog scheme reads $u_{t+1} = u_{t-1} + 2 \times dtF(u_t)$, where the index denotes the time step and the function F represents the different terms driving the evolution of the velocity. In a model where the first layer remains thick, all the terms represented by F have the same order of magnitude. Here we must distinguish between the terms that are proportional to h^0, hereafter $F(u_t)$, and those proportional to h^{-1}, hereafter $h^{-1}G(u_t)$, the latter becoming dominant when the first-layer thickness decreases.

We thus pose the following:

$$u_{1,t+1} = u_{1,t-1} + 2(h_{1,t}/a)\exp(-a\ dt/h_{1,t})\sinh(adt/h_{1,t}) \times [F(u_{1,t}) + h_{1,t}^{-1}G(u_{1,t})]$$

When $h_{1,t}$ remains larger than 10 m, $a\ dt/h_{1,t}$ is much smaller than 1, and the usual leapfrog is obtained. When $h_{1,t}$ tends toward 0, $u_{1,t+1} = u_{1,t-1} + G(u_{1,t})/a$. The function $G(u_{1,t})$ being equal to $\kappa_h(u_{2,t}-u_{1,t})+\tau/\rho$, we obtain $u_{1,t+1} \simeq u_{1,t-1}-\kappa_h u_{1,t}/a+\kappa_h u_{2,t}/a+\tau/(a\rho)$. For $a = \kappa_h$, we obtain $u_{1,t+1} \simeq u_{2,t} + \tau/(\kappa_h\rho)$.

The equation characterizing the evolution of u_2 contains a term of Rayleigh damping proportional to $-\kappa_h(u_2 - u_1)/h_2$. When h_1 tends to 0, this term must become close to $\tau/(\rho h_2)$ because the wind exerts the stress directly onto the second layer. With the previous expression of $u_{1,t+1}$, this property is verified.

REFERENCES

Bryan, F. O., M. W. Hecht, and R. D. Smith. 2007. Resolution convergence and sensitivity studies with North Atlantic circulation models. Part I: The western boundary current system. Ocean Modell., *16*, 141–159.

Charney, J. G. 1955. The Gulf Stream as an inertial boundary layer. Proc. Natl. Acad. Sci. U. S. A., *41*, 731–740.

Chassignet, E., and R. Bleck. 1993. The influence of layer outcropping on the separation of boundary currents. Part I: The wind-driven experiments. J. Phys. Oceanogr., *23*, 1485–1507.

Chassignet, E., R. Bleck, and C. G. H. Rooth. 1995. The influence of layer outcropping on the separation of boundary currents. Part II: The wind- and buoyancy-driven experiments. J. Phys. Oceanogr., *25*, 2404–2422.

Cessi, P. 1990. Recirculation and separation of boundary currents. J. Mar. Res., *48*, 1–35.

Cessi, P., R. V. Condie, and W. R. Young. 1990. Dissipative dynamics of western boundary currents. J. Mar. Res., *48*, 677–700.

Cessi, P., and S. Louazel. 2001. Decadal oceanic response to stochastic wind forcing. J. Phys. Oceanogr., *31*, 3020–3029.

Cushman-Roisin, B., L. Pratt, and E. Ralph. 1993. A general theory for equivalent barotropic thin jets. J. Phys. Oceanogr., *23*, 91–103.

de Coëtlogon, G., C. Frankignoul, M. Bentsen, C. Delon, H. Haak, A. Paerdens, S. Masima, and A. Paerdens. 2006. Gulf Stream variability in five oceanic general circulation models. J. Phys. Oceanogr., *36*, 2119–2135.

Février, S., J. Sirven, and C. Herbaut. 2007. Interaction of a coastal Kelvin wave with the mean state in the Gulf Stream separation area. J. Phys. Oceanogr., *37*, 1429–1444.

Frankignoul, C., G. de Coëtlogon, T. M. Joyce, and S. Dong. 2001. Gulf Stream variability and ocean–atmosphere interactions. J. Phys. Oceanogr., *31*, 3516–3529.

Gerdes, R., and C. Köberle. 1995. On the influence of DSOW in a numerical model of the North Atlantic general circulation. J. Phys. Oceanogr., *25*, 2624–2642.

Halkin, D., and T. Rossby. 1985. The structure and transport of the Gulf Stream at 73°W. J. Phys. Oceanogr., *15*, 1439–1452.

Hameed, S., and S. Piontkovski. 2004. The dominant influence of the Icelandic Low on the position of the Gulf Stream northwall. Geophys. Res. Lett., *31*, L09303, doi: 10.1029/2004GL019561

Huang, R. X., and G. R. Flierl. 1987. Two-layer models for the thermocline and current structure in subtropical/subpolar gyres. J. Phys. Oceanogr., *17*, 872–884.

Joyce, T. M., C. Deser, and M. A. Spall. 2000. The relation between decadal variability of subtropical mode water and the North Atlantic Oscillation. J. Clim., *13*, 2550–2569.

Kelly, K. A., S. Singh, and R. X. Huang. 1999. Seasonal variations of sea surface height in the Gulf Stream region. J. Phys. Oceanogr., *29*, 313–327.

Kiss, A. E. 2002. Potential vorticity "crises", adverse pressure gradients, and western boundary current separation. J. Mar. Res., *60*, 779–803.

Kwon Y.-O., M. A. Alexander, N. A. Bond, C. Frankignoul, H. Nakamura, B. Qiu, and L. A. Thompson. 2010. Role of the Gulf Stream and Kuroshio–Oyashio systems in large-scale atmosphere–ocean interaction: A review. J. Clim., *23*, 3249–3281.

Kwon, Y.-O., and C. Frankignoul. 2012: Stochastically-driven multidecadal varaibility of the Atlantic meridional overturning circulation in CCSM3. Clim. Dyn., *38*, 859–876.

Kwon, Y.-O., and C. Frankignoul. 2014: Mechanisms of multidecadal Atlantic meridional overturning circulation varaibility diagnosed in depth versus density space. J. Clim., *27*, 9359–9276.

LaCasce, J. H. 1980. Baroclinic Rossby waves in a square basin. J. Phys. Oceanogr., *30*, 3161–3178.

Lumpkin, R., and K. Speer. 2007. Global ocean meridional overturning. J. Phys. Oceanogr., *37*, 2550–2562.

Marshall, J., H. Johnson, and J. Goodman. 2001. A study of the interaction of the North Atlantic Oscillation with ocean circulation. J. Clim., *14*, 1399–1421.

Marshall, J., and G. Nurser. 1988. On the recirculation of the subtropical gyre. Q. J. R. Meteorol. Society., *114*, 1517–1534.

Nurser, A. J. G., and R. G. Williams. 1990. Cooling Parsons' model of the separated Gulf Stream. J. Phys. Oceanogr., *20*, 1974–1979.

Özgökmen, T. M., E. P. Chassignet, and A. M. Paiva. 1997. Impact of wind forcing, bottom topography, and inertia on midlatitude jet separation in a quasigeostrophic model. J. Phys. Oceanogr., *27*, 2460–2476.

Parsons, A. T. 1969. A two-layer model of Gulf Stream separation. J. Fluid Mech., *39 (3)*, 511–528.

Pedlosky, J. 1987. On Parsons' model of the ocean circulation. J. Phys. Oceanogr., *17*, 1571–1582.

Peña-Molino B., and T. M. Joyce. 2008. Variability in the Slope Water and its relation to the Gulf Stream path. Geophys Res. Lett., *35*, L03606, doi: 10.1029/2007/GL032183

Primeau, F. W., and D. Newman. 2007. Bifurcation structure of a wind-driven shallow water model with layer-outcropping. Ocean Modell., *16*, 250–263.

Rossby, T., and R. L. Benway. 2000. Slow variations in mean path of the Gulf Stream east of Cape Hatteras. Geophys Res. Lett., *27*, 117–120.

Rossby, T., C. Flagg, and K. Donohue. 2005. Interannual variations in upper-ocean transport by the Gulf Stream and adjacent waters between New Jersey and Bermuda. J. Mar. Res., *63*, 203–226.

Rossby, T., C. N. Flagg, and K. Donohue. 2010. On the variability of Gulf Stream transport from seasonal to decadal timescales. J. Mar. Res., *68*, 503–522.

Sadourny, R. 1975. The dynamics of finite-difference models of the shallow-water equations. J. Atmos. Sci., *32*, 680–689.

Sasaki, Y. N., S. Minobe, and N. Schneider. 2013. Decadal response of the Kuroshio Extension jet to Rossby waves: Observation and thin-jet theory. J. Phys. Oceanogr., *43*, 442–456.

Sasaki, Y. N., and N. Schneider, 2011a: Decadal shifts of the Kuroshio Extension jet: Application of thin-jet theory. J. Phys. Oceanogr., *41*, 979–993.

Sasaki, Y. N., and N. Schneider, 2011b: Interannual to decadal Gulf Stream variability in an eddy-resolving ocean model. Ocean Modell, *39*, 209–219.

Shimokawa, S., and T. Matsuura. 2010. chaotic behaviours in the response of a quasigeostrophic oceanic double gyre to seasonal external forcing. J. Phys. Oceanogr., *40*, 1458–1472.

Simonnet, E., M. Ghil, K. Ide, R. Temam, S. Wang. 2003a. Low-frequency variability in shallow-water models of the wind-driven ocean circulation. Part I: Steady-state solutions. J. Phys. Oceanogr., *33*, 712–728.

Simonnet, E., M. Ghil, K. Ide, R. Temam, S. Wang. 2003b. Low-frequency variability in shallow-water models of the wind-driven ocean circulation. Part II: Time-dependent solutions. J. Phys. Oceanogr., *33*, 729–752.

Sirven, J. 2005. Response of the separated western boundary current to harmonic and stochastic wind stress variations in a 1.5-layer ocean model. J. Phys. Oceanogr., *35*, 1341–1358.

Sirven, J., C. Herbaut, J. Deshayes, and C. Frankignoul. 2007. Origin of the annual to decadal peaks of variability in the response of simple ocean models to stochastic forcing. J. Phys. Oceanogr., *37*, 2146–2157.

Spall, M. A. 1996a. Dynamics of the Gulf Stream/deep western boundary current crossover. Part I: Entrainment and recirculation. J. Phys. Oceanogr., *26*, 2152–2168.

Spall, M. A. 1996b. Dynamics of the Gulf Stream/deep western boundary current crossover. Part II: Low-frequency internal oscillations. J. Phys. Oceanogr., *26*, 2169–2182.

Talley, L. D., J. L. Reid, and P. E. Robbins. 2003. Data-based meridional overturning streamfunctions for the global ocean. J. Clim., *16*, 3213–3226.

Taylor, A. H., and J. A. Stephens. 1998. The North Atlantic Oscillation and the latitude of the Gulf Stream. Tellus A, *50*, 134–142.

Thompson, J. D., and W. J. Schmitz Jr. 1989. A limited-area model of the Gulf Stream: Design initial experiments, and model-data intercomparison. J. Phys. Oceanogr., *19*, 791–814.

Uppala, S. M., P. W. Kållberg, A. J. Simmons, U. Andrae, V. da Costa Bechtold, M. Fiorino, J. K. Gibson, et al. 2005. The ERA-40 re-analysis. Q. J. R. Meteorol. Soc., *131*, 2961–3012. doi: 10.1256/qj.04.176

Worthington, L. V. 1976. On the North Atlantic Circulation. Baltimore: Johns Hopkins University Press, 110 pp.

Zhang, R., and G. K. Vallis. 2007. The role of bottom vortex stretching on the path of the North Atlantic western boundary current and on the northern recirculation gyre. J. Phys. Oceanogr., *37*, 2053–2080.

Received: *15 August 2012*; revised: *9 July 2015*.